



Article

Laser-Plasma Spatio-Temporal Cyanide Spectroscopy and Applications

Christian G. Parigger^{1,*} , Christopher M. Helstern¹, Benjamin S. Jordan², David M. Surmick³ , Robert Splinter⁴

¹ Physics and Astronomy Department, University of Tennessee, University of Tennessee Space Institute, Center for Laser Applications, 411 B.H. Goethert Parkway, Tullahoma, TN 37388-9700, USA

² Nuclear Engineering Department, University of Tennessee, Tickle College of Engineering, 1412 Circle Drive, Knoxville, TN 37912, USA

³ Physics and Applied Physics Department, University of Massachusetts Lowell, Lowell, MA 01854, USA

⁴ Welling Medical, Van der Waals Park 22, 9351 VC Leek, The Netherlands

* Correspondence: cparigge@tennessee.edu; Tel.: +1 (931)-841-5690

Abstract: This article reports new measurements of laser-induced plasma hypersonic expansion measurements of diatomic molecular cyanide (CN). Focused, high-peak power 1064-nm Q-switched radiation of the order of 1 TW/cm² generates optical breakdown plasma in a cell containing a 1:1 molar gas mixture of N₂ and CO₂ at a fixed pressure of 1.1×10^5 Pascal and in a 100 ml/min flow of the mixture. Line-of-sight (LOS) analysis of recorded molecular spectra indicate the outgoing shockwave at expansion speeds well in excess of Mach number 5. Spectra of atomic carbon confirm an increased electron density near the shock wave, and equally, molecular CN spectra reveal higher excitation temperature near the shockwave. The results are consistent with corresponding high-speed shadow graphs obtained by visualization with an effective shutter speed of five nanoseconds. In addition, LOS analysis and application of integral inversion techniques allow inferences about the spatio-temporal distribution of the plasma.

Keywords: Plasma diagnostics; molecular spectra; diatomic molecules; plasma spectroscopy; laser spectroscopy; laser-induced breakdown spectroscopy; optical emission spectroscopy; hypersonic expansion

1. Introduction

Molecular recombination spectra are readily measured following optical breakdown in gases, the cyanide (CN) molecule can be recognized rather early for time delays of the order of 100 ns after cessation of the laser pulse [1]. Gas mixtures are selected for the purpose of measuring CN spatio-temporal distributions associated with high-speed, hypersonic gas-dynamic expansion. Applications of cyanide spectroscopy include various scientific areas including medical research and selected engineering endeavors.

Cyanides are connected to many living organisms and are created through man-made processes, but they are highly toxic. Human exposures can occur through accidental ingestion or inhalation of cyanides. Synthetic materials can be found in 21st century buildings and furnishings which produce toxic combustion byproducts, like hydrogen cyanide (HCN), when burned [2]. Victims of these fires can have significant intakes of HCN, which can lead to cyanide poisoning and ultimately death. Cyanide detection can identify cyanide poisoning occurrences in humans and can assist in determination of adequate treatment. Additionally, HCN can be produced by bacteria such as *Pseudomonas aeruginosa* [3]. Immune-compromised patients such as those with cystic fibrosis (CF) are susceptible to increased

morbidity and mortality when afflicted by these bacteria [3]. Detection of bacterial produced HCN in the airways will lead to earlier treatment of immune-compromised infected with these bacteria.

The diatomic molecule CN has remained a target for improved detection capability and deeper understanding largely because engineers cannot replicate CN's effectiveness for certain industrial applications with any other compound. For example, 90% of the gold mining operations world-wide utilize CN because of its availability, effectiveness, and cost efficiency [4]. Although accidents, injuries, and environmental mishaps are possible, when they occur, they require specialized detection capability to ensure safety of the workers during the remediation. The engineering applications associated with plastic manufacturing that continue to use cyanide create a downstream problem for fire fighters, analogous to that of fire victims mentioned above. Fire fighters must go into buildings where the plastics that may have used cyanide during their manufacture are now evolving their constituents into the air as they are consumed by fire [5]. Again, detection and assessment of amount of CN present is needed to help keep fire fighters safe.

Engineers continue to look for a means of obtaining the CN properties that customers need, but that do not have the potential health hazards that are present with CN. Engineers have been seeking ways to lower the cyanide utilization in the nitriles chemical industry [6]. Alternatives to cyanide are also being sought for the mining industry, but this task has proven difficult because the replacement candidates are often not as broadly applicable and must be tailored to the specific ore [7].

In addition, CN is a component of vehicle exhaust [8]. It is important for engineers to continue to research the details of CN detection and evaluation to be able to characterize the relative emission impacts that different vehicles contribute [9]. There is CN production potential in other combustion processes as well, including CN spectroscopy of TNT simulant molecules [10] and continued understanding of what CN production should be expected is going to continue to drive interest and investigation into CN even if engineers are able to replace CN in many industrial applications [11].

2. Experimental details

The standard experimental components are used for laser-induced breakdown spectroscopy and have been summarized previously, e.g., see Ref. [1], but are included for completeness. The experimental arrangement consists of a set of components typical for time-resolved, laser-induced optical emission spectroscopy, or nanosecond laser-induced breakdown spectroscopy (LIBS) [12]. Primary instrumentation includes a Q-switched Nd:YAG device (Quantel model Q-smart 850, US) operated at the fundamental wavelength of 1064-nm to produce full-width-at-half-maximum 6-ns laser radiation with an energy of 850 mJ per pulse, a laboratory type Czerny-Turner spectrometer (Jobin Yvon model HR 640, Fr) with a 0.64-m focal length and equipped with a 1200 grooves/mm grating, an intensified charge coupled device (Andor Technology model iStar DH334T-25U-03, US) for recording of temporally and spatially resolved spectral data, a laboratory chamber or cell with inlet and outlet ports together with a vacuum system, electronic components for synchronization, and various optical elements for beam shaping, steering and focusing.

For the generation of optical breakdown micro-plasma, a singlet lens (Thorlabs model LA1509-C, US) is used close to the top entrance window of one arm of the chamber containing the 1:1 CO₂:N₂ atmospheric molar gas mixture (Airgas ultra-high purity N₂ and research grade CO₂). For 1:1 imaging of the plasma onto the 100 μ m spectrometer slit, a fused silica plano-convex lens (Thorlabs model LA4545, US) is employed. For the CN experiments reported here, the laser pulse energy is attenuated with beamsplitters and apertures from 850 mJ/pulse to 170 mJ/pulse. Measurements are performed with and without an Order Sorting Filter (Oriel model 51250, US) with a cut-on wavelength of 309 nm and transmittance range of 325 nm to evaluate the C I 193.09-nm atomic carbon line in second order interference as identified in previous work [1].

In previous experiments, captured shadowgraphs of the breakdown plasma [13] served the purpose of visualizing the plasma expansion when using 850 mJ, 6-ns radiation. However, it is important to obtain shadowgraphs for plasma excitation energies that were employed for time-resolved

spectroscopy. Shadowgraphs reported in this work are captured using two separate laser devices (Continuum Surelite model SL I-10, US) that can be externally operated to deliver laser pulses with a well-defined time delay showing less than ± 1 ns trigger-jitter between the pulses. For visualization studies, both lasers are frequency-doubled to operate at the 2nd harmonic, 532-nm wavelength, and both beams are spatially overlapped. Both pulses can be delivered with a minimum time delay of 300 ns. Shadowgraphs are recorded by external synchronization of the Surelite and Quantel laser devices and by external triggering the camera (Silicon Video 9C10 color camera, US) that records the images that are projected onto a screen.

3. Results and discussion

3.1. Shadowgraphs

Two typical images are reported here. First, Figure 1 displays a shadowgraph of the IR, 1064-nm laser-induced plasma for an excitation energy of 170 mJ, 6-ns pulse width. The shadowgraph is captured using a single, 5-ns pulse-width 532-nm beam.

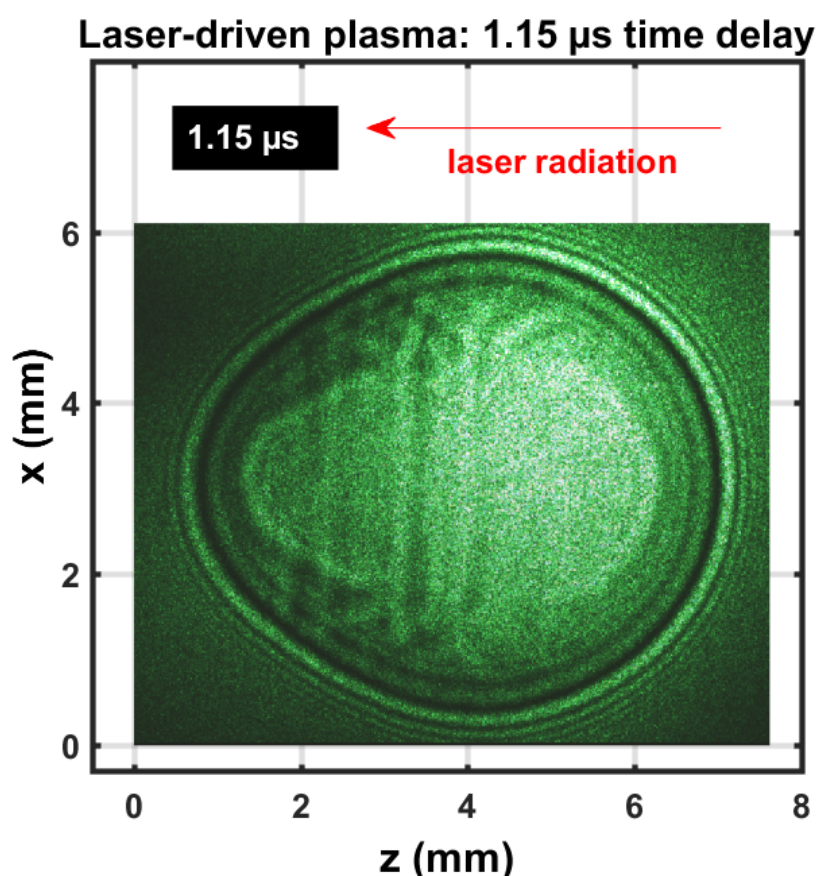


Figure 1. Single-shot shadowgraph of the expanding laser-induced plasma initiated with a 170-mJ, 6-ns, 1064-nm focused beam, and imaged using a 5-ns, 532-nm back-light that is time-delayed by $1.15 \mu\text{s} \pm 0.05 \mu\text{s}$.

The expanding shock-wave is clearly visible, including the central plasma kernel. The image is nearly spherical, previously reported shadowgraphs that utilize 850-mJ excitation would reveal stronger deviation from spherical symmetry than the images obtained with 170 mJ/pulse. The

expanding shockwave radius is consistent with previous assessments of hypersonic laser-plasma expansion images [13] that employ the Taylor-Sedov energy^{1/5} dependency [14],

$$R(\tau) = \left(\frac{E}{\rho} \tau^2 \right)^{1/5}, \quad (1)$$

of the shockwave radius, $R(t)$, as function of the absorbed pulse energy, E , density of the gas, ρ , and the time delay, τ . Tables 1 and 2 compare for energies of 160 mJ and 200 mJ, respectively, computed blast-wave radii for standard ambient temperature and pressure (SATP) air and the CN mixture. Consequently, measured shadowgraphs in air provide an excellent guide for the gaseous mixture.

Table 1. Computed shockwave radii for SATP air and for the molar CN mixture, 160 mJ.

time delay (ns)	r(mm) for air [$\rho = 1.2 \text{ kg/m}^3$]	r(mm) for CN mix [$\rho = 1.63 \text{ kg/m}^3$]
200	1.40	1.31
450	1.93	1.82
700	2.31	2.17
950	2.61	2.45
1200	2.86	2.69
1450	3.09	2.90

Table 2. Computed shockwave radii for SATP air and for the molar CN mixture, 200 mJ.

time delay (ns)	r(mm) for air [$\rho = 1.2 \text{ kg/m}^3$]	r(mm) for CN mix [$\rho = 1.63 \text{ kg/m}^3$]
200	1.46	1.37
450	2.02	1.90
700	2.41	2.27
950	2.73	2.56
1200	2.99	2.81
1450	3.23	3.04

And second, Figure 2 exhibits a composite shadowgraph obtained by initiating laser-plasma with the first, green, 90 mJ/pulse, 5-ns beam, and subsequently, initiating laser plasma at the shockwave with the second, green, 110 mJ/pulse, 5-ns beam that exactly overlaps spatially, but is time delayed by $0.45 \mu\text{s}$. The composite image is obtained with the $0.45 \mu\text{s}$ time delay and an extra 30-ns optical time delay for each beam. The initial, elongated multiple-breakdown in the central region is imaged with the first 5-ns pulse-width beam. The near-spherical shockwave is imaged with the second 5-ns pulse-width beam and the corresponding 30-ns time delayed beam. However, the second beam initiates breakdown at the forward side (left in the image) and at the side of the incoming beam (right in the image) indicated by a dark ring – the extent of that dark ring is due to the use of a 5-ns pulse-width beam, time-delayed by 30 ns for shadowgraph capture of the expansion dynamics. The expansion speed of the second optical breakdown at the right of the image is well over one order of magnitude larger than hypersonic speed in SATP air.

A subsidiary measurement utilized a pyroelectric laser-pulse energy meter (Scientech model P50, US) for determination of absorbed energy for the laser-induced plasma studies. The transmitted energy per pulse, E_t , amounted to $20 \pm 3 \text{ mJ}$ for IR laser-induced plasma studies. This energy/pulse represents the optical breakdown threshold. The energy/pulse threshold corresponds to the peak-power per area or irradiance threshold for SATP air optical breakdown [15]. For example, for perfect Gaussian beam focusing [16,17] with $f/20$, i.e., $F/D = 20$ with F and D denoting respectively the focal length and the beam diameter at the lens, for 1064-nm IR wavelength, λ , and from the beam radius, w_0 ,

$$w_0 = \frac{2}{\pi} \lambda \frac{F}{D}, \quad (2)$$

one finds the focal area of $5.8 \times 10^{-6} \text{ cm}^2$. Using for $\Delta\tau_{\text{pulse}} = 6 \text{ ns}$ pulses the peak-power, $\frac{1}{2}E_t/\Delta\tau_{\text{pulse}}$, of 1.7 MW (mean-field top-hat model for the temporal pulse distribution) one would find the irradiance threshold of $2.9 \times 10^{11} \text{ GW/cm}^2$. In view of Equation 1 for determination of the shockwave radius, the absorbed energy per pulse should be used. However, the 1/5-exponent implies diminished dependency on the energy/pulse when in the range of 160 mJ and 200 mJ as displayed in Tables 1 and 2. In other words, a ratio of $220/200 = 1.1$ or a 10% difference in energy/pulse would result in a 2% difference in the predicted shockwave radius for the same density and time delay.

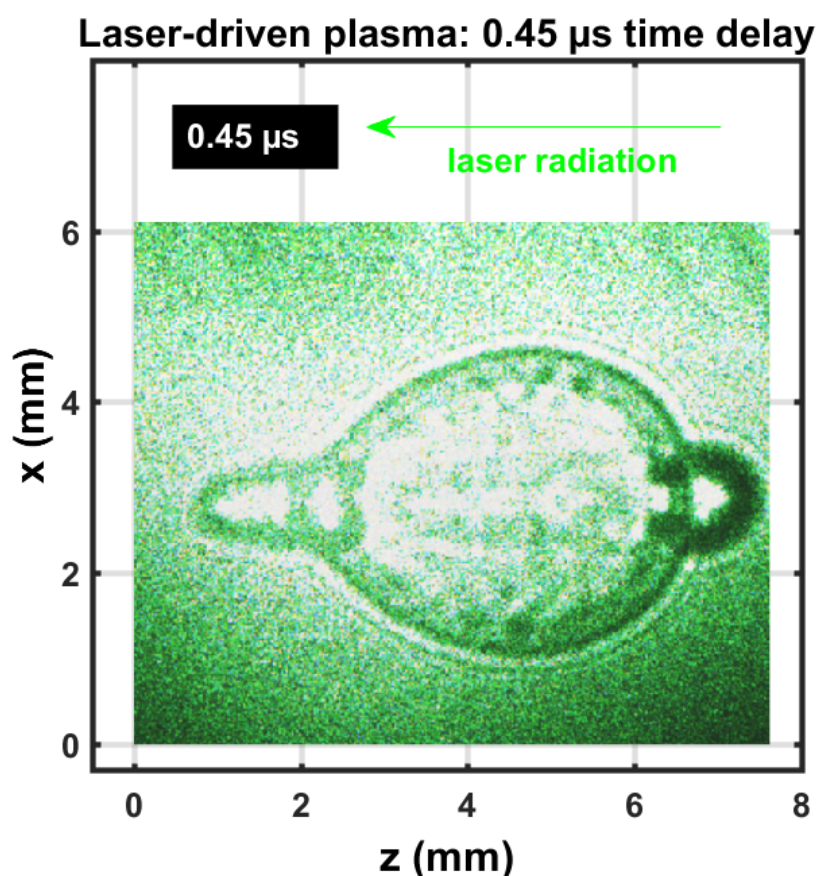


Figure 2. Single-shot shadowgraph of laser-induced plasma initiated with 90-mJ and 110-mJ, 5-ns, 532-nm focused beams, and imaged using two 5-ns, 532-nm back lights that are time-delayed by 0.03 μs , 0.45 μs , and 0.48 μs .

3.2. Cyanide spectra

The experimental series for the measurement of the CN molecular distribution after optical breakdown includes evacuating the cell to a nominal backing pump pressure of the order of 1 Pa (10^{-2} Torr), followed by generating the mixture from ultra-high pure N_2 and research grade CO_2 . Optical breakdown was generated inside the chamber at a rate of 10 Hz, with the laser beam focused with f/5 optics from the top, or parallel to the slit. The detector pixels are binned in 4-pixel tracks along the slit direction, resulting in obtaining 256 spectra for each time delay. Recording of measurements with and without the Order-Sorting filter consist of 100 accumulations collected for 21 time delays at 250 ns steps. These runs allow for evaluation of CN plasma spatial and temporal characteristics and the CI 193.09-nm atomic carbon line in second order. Figures 3 and 4 illustrate recorded spatio-temporal spectra that were recorded along the line-of-sight and are accumulated over 100 individual laser-plasma events. The slit-height corresponds to the z-direction and the line-of-sight corresponds to the y-direction in reference to Figs. 1 and 2.

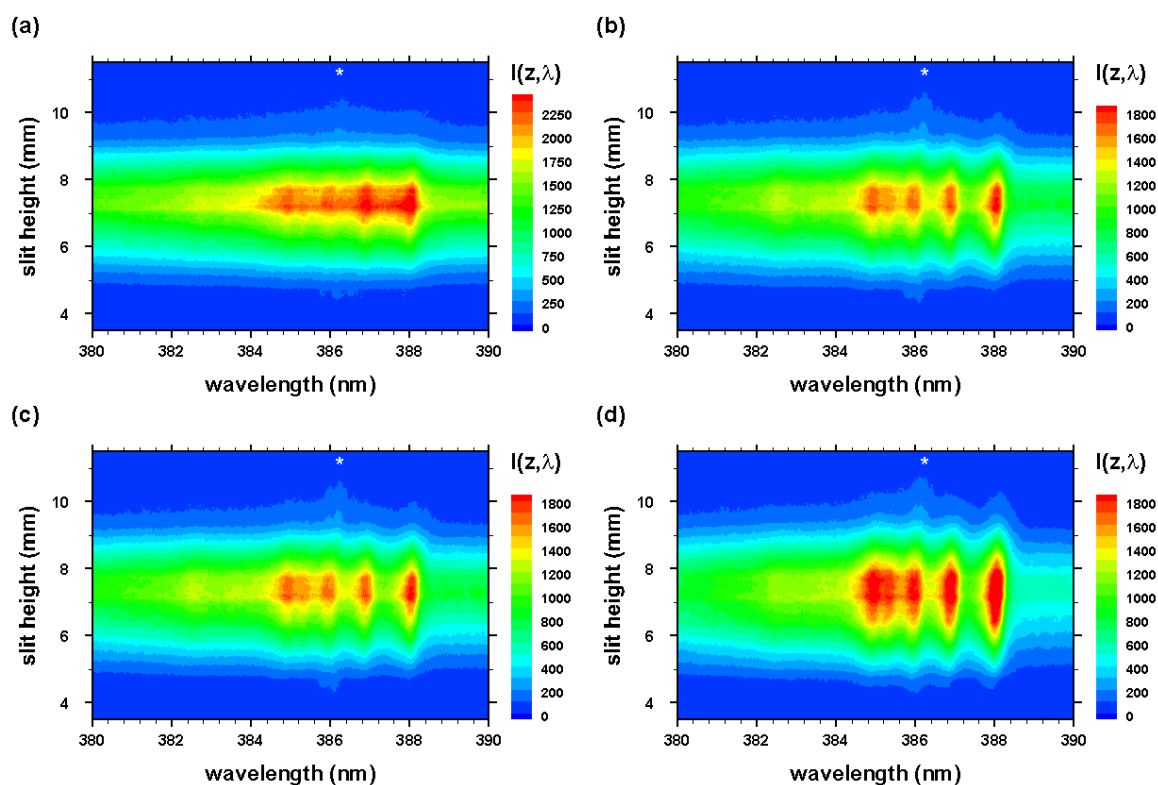


Figure 3. Optical breakdown CN-spectra in a 1:1 molar $\text{CO}_2:\text{N}_2$ atmospheric gas mixture for time delays (a) 200 ns, (b) 450 ns, (c) 700 ns, and (d) 950 ns. Spectrometer-detector gatewidth: 125 ns. The asterisk, *, indicates the 2nd order, neutral carbon line.

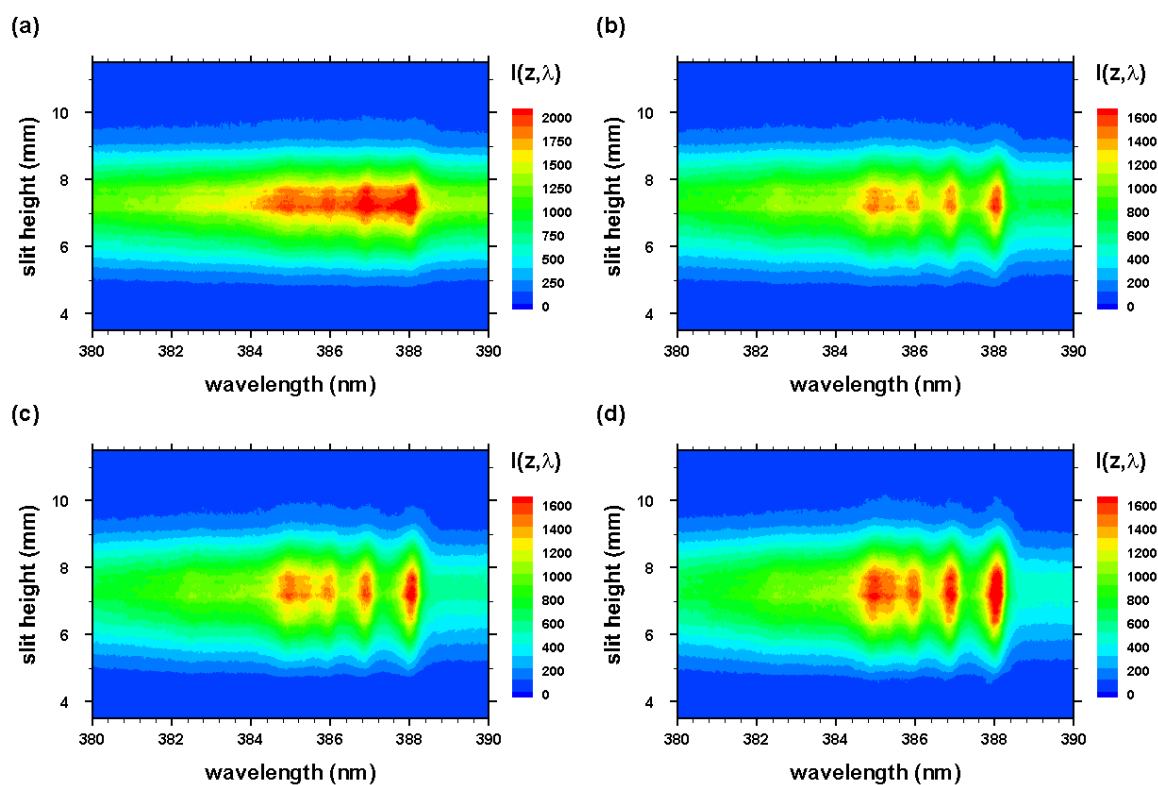


Figure 4. Optical breakdown CN-spectra as in Fig. 3 for time delays (a) 200 ns, (b) 450 ns, (c) 700 ns, and (d) 950 ns, but recorded with a 309-nm cut-on wavelength filter.

3.3. Cyanide temperature

Both line-of-sight and Abel inverted data sets of the CN-spectra are subjected to analysis with the so-called NMT, or Nelder-Mead temperature, program that has been made available along with the required CN-violet system data set [18,19]. Figure 5 illustrates a typical CN-spectrum and fit of line-of-sight data accomplished in this work.

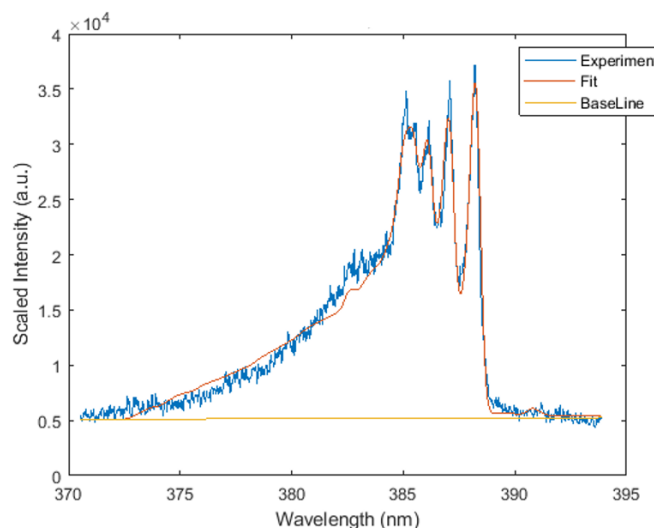


Figure 5. Typical fitted CN spectrum, $T = 8947$ K, fit $FWHM = 0.47$ nm.

Figure 6 exhibits results of the analysis of the filtered, line-of-sight molecular CN-spectra. The figures reveal the occurrence of the outgoing shockwave along with temperature variations in the central region of the plasma. These data of slit-height vs. temperature show increased temperature near the edges.

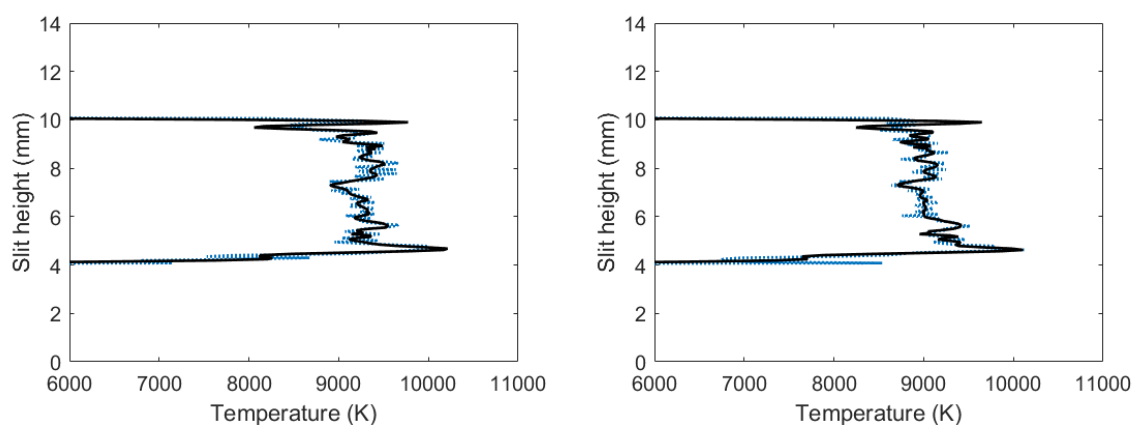


Figure 6. Temperature vs. slit height for filtered CN-spectra (left) 700 ns and (right) 950 ns time delay.

3.4. Electron density

Unfiltered spectra contain an overlap of the CI 193.09-nm atomic carbon line in second order and the 2-2 CN band head of 386.19 nm, where filtered spectra only contain the 2-2 CN band head of 386.19 nm. CI 193.09-nm atomic carbon line in second order Stark widths were evaluated for filtered and unfiltered spectra using peak fitting programs. The difference between the filtered and unfiltered spectra is obtained by applying deconvolution. Figure 7 illustrates the results for the widths at full-width-half maximum of the carbon peak. Figure 7 reveals that larger Stark widths are seen near the edges of the plasma, while smaller Stark widths are near the center of the plasma.

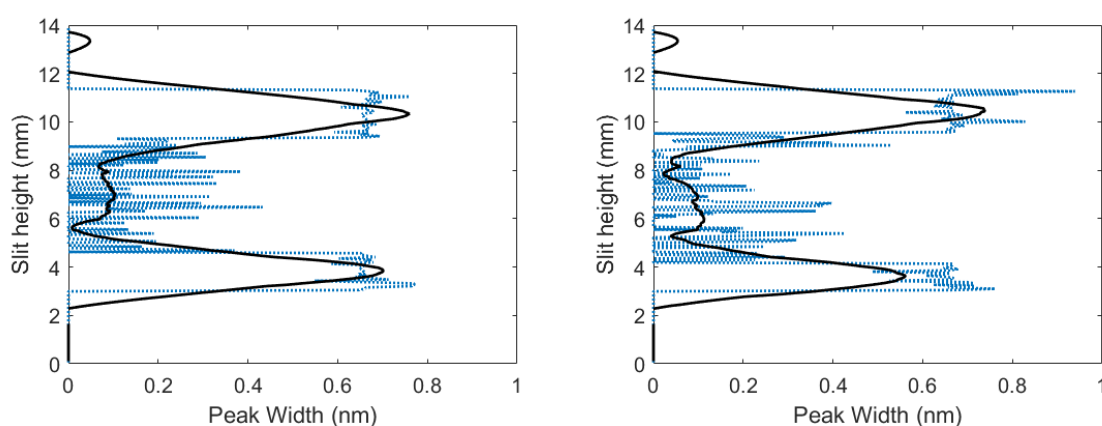


Figure 7. Inferred widths of CI 193.09-nm atomic carbon line in second-order vs. slit height for time delays of (left) 700 ns and (right) 950 ns.

The electron number density, n_e , can be determined from the Stark full-width at half maximum, $\Delta\lambda_{\text{Stark}}$, of the CI 193.09-nm atomic carbon line [20], measured in 2nd order,

$$\Delta\lambda_{\text{Stark}}(\text{nm}) = 2w(\text{nm}) n_e(10^{17}\text{cm}^{-3}), \quad (3)$$

where the width parameter, w , is extrapolated [20,21] to amount to $w \approx 0.0029$ nm. Figure 8 displays the calculated electron densities versus slit height. The calculated electron densities are of the order of $n_e \approx 10^{17}\text{cm}^{-3}$ in the central region. Higher electron densities are seen near the edges of the plasma, while smaller electron densities are near the center of the plasma.

Using the Taylor-Sedov blast wave model (see Equation 1), the radius of the plasma, R_{plasma} , at time delay of 450 ns is ≈ 1.9 mm which would indicate higher electron density near the shockwave, which is consistent with the results shown in Figure 8.

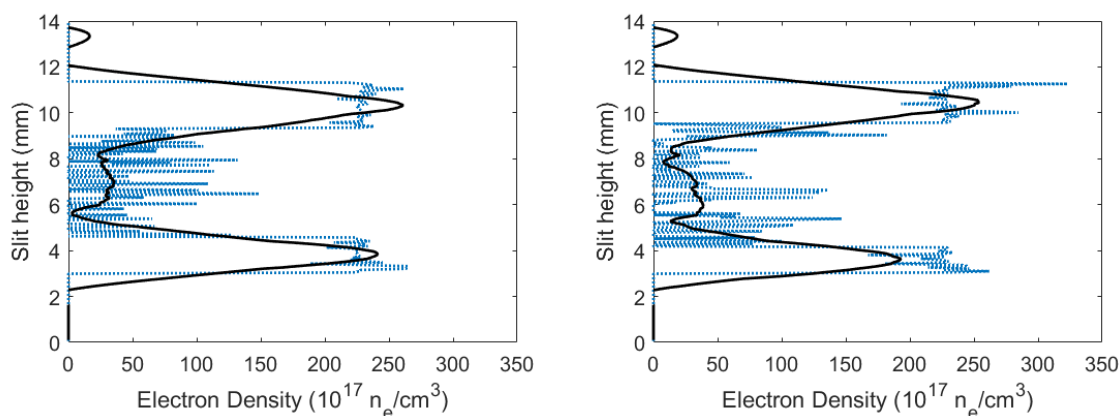


Figure 8. Calculated electron densities versus slit height for time delays of (left) 450 ns and (right) 950 ns.

3.5. Cyanide spectra in flowing gas

The experimental series for the measurement of the CN molecular distribution after optical breakdown for the flowing gas mixture utilizes a similar process as discussed in the previous sections. The experiments include supplying the cell with a constant flow of the ultra-high pure N₂ and research grade CO₂ gas mixture instead of a fixed volume of the mixture. The flowrate of the mixture entering and leaving the cell is 100 mL/min and is monitored using a flowmeter (Cole-Parmer FM 112-02ST). Optical breakdown was generated inside the chamber at a rate of 10 Hz, with the laser beam focused with f/5 optics from the top, or parallel to the slit. The detector pixels are binned in 4-pixel tracks along

the slit direction, resulting in obtaining 256 spectra for each time delay. Recording of measurements with and without the Order-Sorting filter consist of 100 accumulations collected for 21 delays at 250 ns steps.

Applying the NMT program to the filtered, line-of-sight molecular CN-spectra produced in the flowing gas mixture yields results shown in Figure 9. The figure reveals the occurrence of the outgoing shockwave along with temperature variations in the central region of the plasma and these data of slight-height vs. temperature show increased temperatures near the edges analogous to the results with the fixed amount of gas mixture. Comparing these results to Figure 7, CN calculated temperatures for a fixed amount of gas mixture, it appears that the highest calculated CN temperatures for Figure 7 are towards the bottom of the plasma, where the highest calculated CN temperatures for the flowing gas are towards the top of the plasma.

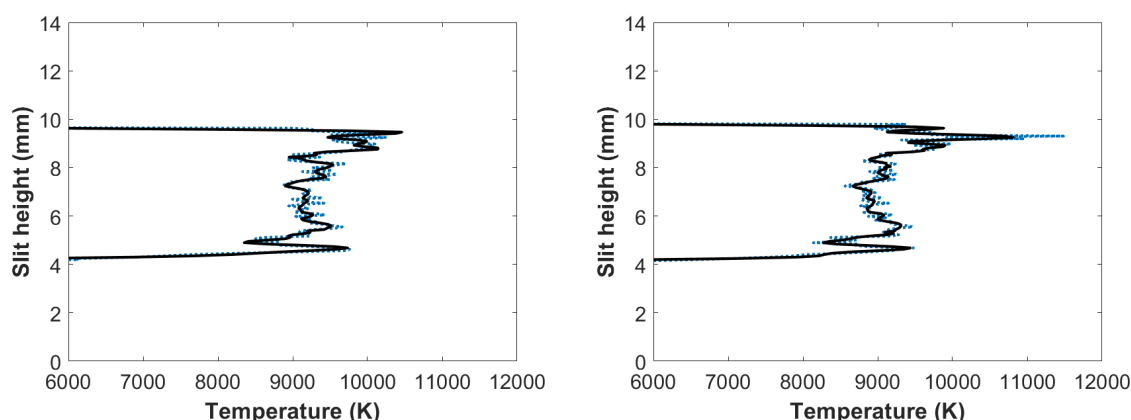


Figure 9. Temperature vs. slit height for flowing gas filtered CN-spectra (left) 700 ns (right) 950 ns time delay.

Just as in the fixed gas mixture, unfiltered spectra contain an overlap of the CI 193.09-nm atomic carbon line in second order and the 2-2 CN band head of 386.19 nm, where filtered spectra only contain the 2-2 CN band head of 386.19 nm. The CI 193.09-nm atomic carbon line in second-order Stark widths were evaluated for filtered and unfiltered spectra using peak fitting programs and the difference between the filtered and unfiltered spectra is obtained by applying deconvolution. Figure 10 illustrates the results for the width at full-width-half-maximum of the carbon peak and reveal that larger Stark widths are seen near the edges of the plasma, while smaller Stark width are near the center the plasma similar to the results in the fixed gas mixture.

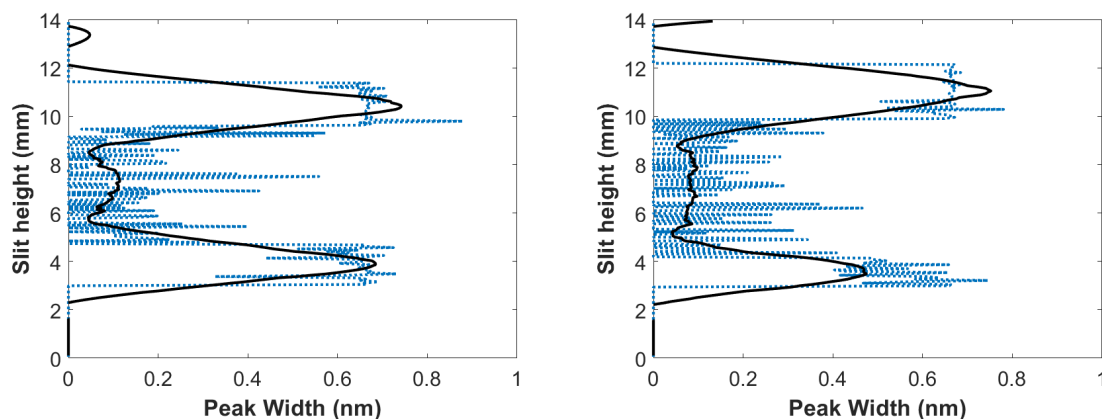


Figure 10. CN flowing gas inferred widths of CI 193.09-nm atomic carbon line in second-order vs. slit height for time delays of (left) 700 ns and (right) 950 ns.

Using Equation 3, electron densities can be calculated for the flowing gas mixture. Figure 11 displays the calculated electron densities versus slit height and the electron densities are on the order of $\approx 10^{17} \text{ cm}^{-3}$ in the central region. Higher electron densities are seen toward the edges of the plasma and smaller electron densities are near the center of plasma analogous to the results for the fixed gas mixture. Additionally, the plasma at 450 ns delay in Figure 11 displays higher electron densities near the shockwave (at $\approx 1.9 \text{ mm}$), which is consistent with the Taylor-Sedov blast wave model and presented results of experiments with fixed gas mixture in the cell.

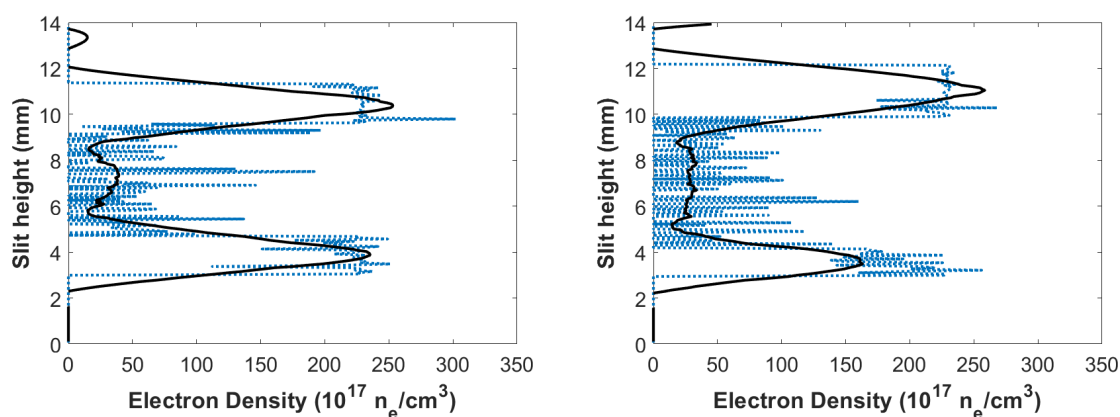


Figure 11. CN flowing-gas calculated electron densities vs. slit height for time delays of (left) 450 ns and (right) 950 ns.

3.6. Abel inverted spectra

In view of the shadowgraphs that are recorded in the $0.5 \mu\text{s}$ to $1 \mu\text{s}$ range (see Figs. 1 and 2) it would be acceptable to apply an Abel inverse transform. Deviation from spherical symmetry is minimal for time delays of the order of $1 \mu\text{s}$ provided laser-induced excitation is accomplished with nanosecond IR radiation of the order of 200 mJ/pulse or less. The analysis of the molecular CN spectra follows the same symmetrization methods as applied for atomic hydrogen spectra [22,23].

The use of Chebyshev polynomials for Abel inversion of the integral equation,

$$I(z, \lambda) = 2 \int_z^{\rho} \varepsilon(r, \lambda) \frac{r}{\sqrt{r^2 - z^2}} dr, \quad (4)$$

allows one to directly invert measured data. The z -direction corresponds to the slit-height, and the line-of-sight integration is along the y -direction in view of Figure 1. In this work, the choice of the number of 15 polynomials for the inversion [24,25] maintains fidelity of the spectra and is equivalent to the use of a digital filter resulting in broadening of the computed radial spectra. A smaller number of polynomials would cause smaller spectral resolution. The measured, line-of sight data, $I(z, \lambda)$, along the slit dimension, z , are inverted for each wavelength, λ , to obtain the radial intensity distribution, $\varepsilon(r, \lambda)$, with the upper limit much larger, $\rho \gg R_{\text{plasma}}$, than the radius, R_{plasma} , of the plasma.

The radial spectra are computed from the 2-dimensional line-of-sight data (see Figs. 3 and 4) that were accumulated with an intensified camera attached to the spectrometer that allows one to resolve spectra along the slit. The recorded data are calibrated, corrected for the system sensitivity using standard lamps, and prepared for Abel inversion. Usually, when recording 2-D spectra, slight wavelength variations towards the edges of the slit occur, but these variations have been taken care of in preparing the data for Abel inversion. Figures 12 and 13 illustrate computed Abel inverted spectra. Only subtle differences may be recognizable near the 2-2 CN band edge due to the CI line when comparing Figs. 12 and 13, however, Fig. 12 also contains electron-density information that confirms higher electron density near the edges than the central regions, and consequently, higher electron temperature for adiabatic expansion.

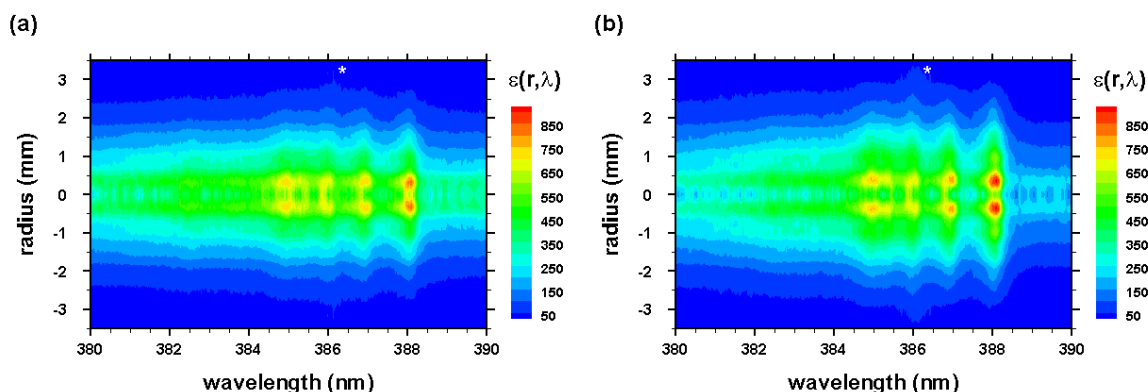


Figure 12. Abel inverted data of Figure 3 for time delays of (a) 450 ns and (b) 950 ns. The asterisk, *, indicates the 2nd order, neutral carbon line.

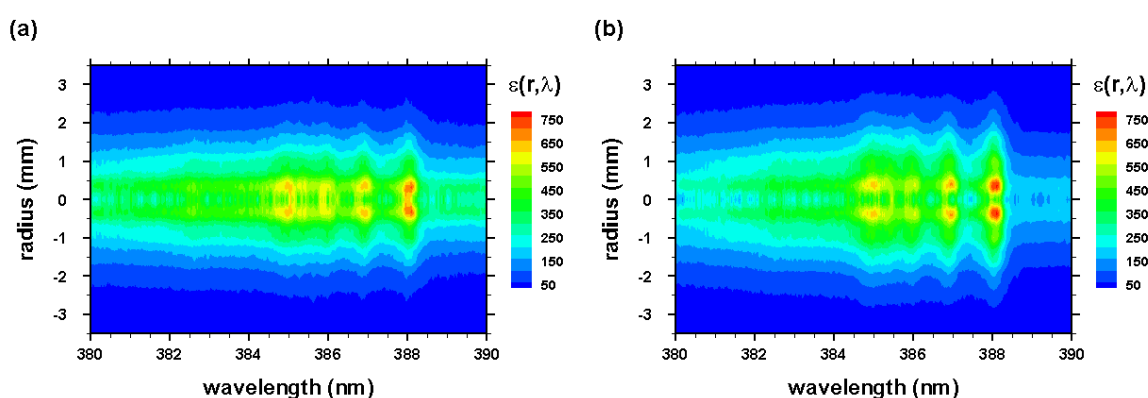


Figure 13. Abel inverted data of Figure 4 for time delays of (a) 450 ns and (b) 950 ns.

Analysis of the Abel-inverted data is expected to reveal similar results for the shock wave, however, in view of the shadowgraphs in Figs. 1 and 2, variations of the CN distribution inside the shockwave and inside the plasma kernel are anticipated.

4. Conclusions

Laser-plasma expansion following optical breakdown occurs at well above hypersonic speed. Measurements of recombination CN-spectra within the first few microseconds yields results as expected from atomic hydrogen, Balmer series laser spectroscopy: The analysis reveals higher electron and higher CN-excitation temperature near the shockwave than in the central region for time delays of the order of one microsecond. The expansion characteristics are deduced from a systematic analysis of the recorded line-of-sight spectra. Application of Abel inversion is reasonable and supported by shadowgraphs recorded in SATP air for laser-plasma initiation for similar energy/pulse as utilized for measurements of molecular spectra.

Author Contributions: All authors contributed equally to this work.

Funding: This research received no external funding.

Acknowledgments: Three of us (CGP, CMH, BSJ) authors wish to acknowledge the support in part by the Center for Laser Applications at the University of Tennessee Space Institute.

Conflicts of Interest: The authors declare no conflict of interest.

References

- Parigger, C.G., Helstern, C.M., Gautam, G. Molecular Emission Spectroscopy of Cyanide in Laser-induced Plasma. *Int. Rev. At. Mol. Phys.* **2017**, *8* (1), 25–35.
- Fent, K.W., Evans, D.E., Babik, K., Striley, C., Bertke, S., Kerber, S., Smith, D., Horn, G.P. Airborne contaminants during controlled residential fires. *J. Occup. Environ. Hyg.* **2018**, *15*, 399–412.
- Arslanov, D.D., Castro, M.P.P., Creemers, N.A., Neerinx, A.H., Spunei, M., Mandon, J., Cristescu, S.M., Merkus, P., Harren, F.J.M. Optical parametric oscillator-based photoacoustic detection of hydrogen cyanide for biomedical applications. *J. Biomed. Opt.* **2013**, *18*, 107002.
- Mudder, T.I., Botz, M.M. Cyanide and society: a critical review. *Eur. J. Miner. Process. Environ. Protect.* **2004**, *4*, 62–74.
- Bolstad-Johnson, D.M., Burgess, J.L., Crutchfield, C.D., Storment, S., Gerkin, R., Wilson, J.R. Characterization of firefighter exposures during fire overhaul. *Am. Ind. Hyg. Assoc.* **2000**, *61*, 636–641.
- Plass, C., Hinzmann, A., Terhorst, M., Brauer, W., Oike, K., Yavuzer, H., Asano, Y., Vorholt, A., Betke, T., Gröger, H. Approaching Bulk Chemical Nitriles from Alkenes: A Hydrogen Cyanide-Free Approach through a Combination of Hydroformylation and Biocatalysis. *Am. Chem. Soc. Catal.* **2019**, *9*, 5198–5203.
- Hilson, G., Monhemius, A.J. Alternatives to cyanide in the gold mining industry: what prospects for the future. *J. Clean. Prod.* **2006**, *14*, 1158–1167.
- Moussa, S.G., Leithead, A., Li, S.-M., Chan, T.W., Wentzell, J.J.B., Stroud, C., Zhang, J., Lee, P., Jeffery, G.L., Brook, R., Hayden, K., Narayan, J., Liggio, J. Emissions of hydrogen cyanide from on-road gasoline and diesel vehicles. *Atmos. Environ.* **2016**, *131*, 185–195.
- Baum, M.M., Moss, J.A., Pastel, S.H., Poskrebyshev, G.A. Hydrogen cyanide exhaust emissions from in-use motor vehicles. *Environ. Sci. Technol.* **2007**, *41*, 857–862.
- Merten, J., Jones, M., Hoke, S., Allen, S. Differential Spectral Imaging of the CN Violet Band in Laser-Induced Plasmas on TNT Simulant Molecules. *Phys.: Conf. Ser.* **2014**, *548*, 012042.
- Dagaut, P., Glarborg, P., Alzueta, M.U. The oxidation of hydrogen cyanide and related chemistry. *Prog. Energ. Combust.* **2008**, *34*, 1–46.
- Cremers, D.A., Radziemski, L.J. Handbook of Laser-Induced Breakdown Spectroscopy, John Wiley & Sons Ltd, US, 2006.
- Gautam, G., Helstern, C.M., Drake, K.A., Parigger, C.G. Imaging of Laser-induced Plasma Expansion Dynamics in Ambient Air. *Int. Rev. At. Mol. Phys.* **2016**, *7*, 45–51.
- Taylor, G.I. The formation of a blast wave by a very intense explosion. - II. The atomic explosion of 1945. *Proc. Roy. Soc. A* **1950** *201*, 175–186.
- Thiyagarajan, M., Thompson, S. Optical breakdown threshold investigation of 1064 nm laser induced air plasmas. *J. Appl. Phys.* **2012**, *111*, 073302.
- Kogelnik, H., Li, T. Laser Beams and Resonators. *Appl. Opt.* **1966**, *5*, 1550–1567.
- Technical Note: Gaussian Beam Optics, <https://www.newport.com/n/gaussian-beam-optics> (accessed on 11 January 2020).
- Parigger, C.G., Woods, A.C., Surmick, D.M., Gautam, G., Witte, M.J., Hornkohl, J.O. Computation of diatomic molecular spectra for selected transitions of aluminum monoxide, cyanide, diatomic carbon, and titanium monoxide. *Spectrochim. Acta Part B: At. Spectrosc.* **2015**, *107*, 32–138.
- Parigger, C.G., Hornkohl, J.O. Quantum Mechanics of the Diatomic Molecule with Applications, IOP Publishing, Bristol, UK, 2019.
- Dackman, M. Laser-Induced Breakdown Spectroscopy for Analysis of High-Density Methane-Oxygen Mixtures, Master's Thesis, University of Tennessee, Knoxville, TN, 2014.
- Griem, H.R. Spectral Line Broadening by Plasmas, Academic Press, New York, USA, 1974.
- Parigger, C.G., Gautam, G., Surmick, D.M. Radial electron density measurements in laser-induced plasma from Abel inverted hydrogen Balmer beta line profiles. *Int. Rev. At. Mol. Phys.* **2015**, *6* (1), 43–55.
- Parigger, C.G., Surmick, D.M., Gautam, G. Self-absorption characteristics of measured laser-induced plasma line shapes. *Phys.: Conf. Ser.* **2017**, *810*, 012012.
- Pretzler, G. A New Method for Numerical Abel-Inversion. *Z. Naturforsch.* **1991**, *46a*, 639–641.
- Pretzler, G., Jäger, H., Neger, T., Philipp, H., Woisetschlager, J. Comparison of Different Methods of Abel Inversion Using Computer Simulated and Experimental Side-On Data. *Z. Naturforsch.* **1992**, *47a*, 955–970.